ACS APPLIED MATERIALS & INTERFACES

www.acsami.org Research Article

Effect of Band Symmetry on Photocurrent Production in Quasi-One-Dimensional Transition-Metal Trichalcogenides

Simeon J. Gilbert, Hemian Yi, Jia-Shiang Chen, Andrew J. Yost, Archit Dhingra, Jehad Abourahma, Alexey Lipatov, Jose Avila, Takashi Komesu, Alexander Sinitskii, Maria C. Asensio, and Peter A. Dowben*

Cite This: *ACS Appl. Mater. Interfaces* 2020, 12, 40525−40531 Read Online

ABSTRACT: Photocurrent production in quasi-one-dimensional (1D) transition-metal trichalcogenides, TiS_3(001) and ZrS_3(001), was examined using polarization-dependent scanning photocurrent microscopy. The photocurrent intensity was the strongest when the excitation source was polarized along the 1D chains with dichroic ratios of 4:1 and 1.2:1 for ZrS_3 and TiS_3, respectively. This behavior is explained by symmetry selection rules applicable to both valence and conduction band states. Symmetry selection rules are seen to be applicable to the experimental band structure, as is observed in polarization-dependent nanospot angle-resolved photoemission spectroscopy. Based on these band symmetry assignments, it is expected that the dichroic ratios for both materials will be maximized using excitation energies within 1 eV of their band gaps, providing versatile polarization sensitive photodetection across the visible spectrum and into the near-infrared.

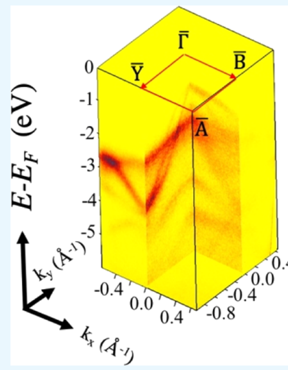

KEYWORDS: *trichalcogenides, phototransistors, 2D materials, band symmetries, polarization dependence*

INTRODUCTION

Transition-metal trichalcogenides (TMTs) are a unique class of two-dimensional (2D) materials that are set apart by their strongly anisotropic optical and electronic properties within their 2D layers.[1−6] This anisotropy is the result of their quasi-one-dimensional (1D) crystal structure in which MX_3 (M = Ti, Zr, Hf, Ta, Nb; X = S, Se, Te) trigonal prisms are formed into 1D chains by strong covalent bonds along the crystallographic $\vec{b}$ axis.[7] These 1D chains then form 2D layers in the $\vec{a}-\vec{b}$ plane through van der Waals-like interactions.[7] Because of their 1D nature, the TMTs have been garnering increasing attention for possible applications in electronics,[5,8−13] optoelectronics,[3−5,14−22] thermoelectrics,[23−26] and energy storage.[27−30] Because of the nature of the chains, the semimetallic and metallic MX_3 trichalcogenides can be scaled to nanometer widths and retain exceptionally high current densities,[31−34] suggesting that these materials may be suitable for devices on the subnanometer scale.

Of particular interest are the strongly polarization-dependent optical properties, which have been demonstrated for both TiS_3(001) and ZrS_3(001).[3−6,20,22,35,36] The polarization-dependent optical properties are promising for the creation of polarization-sensitive photodetectors. Photocurrent measurements, in previous studies, have shown dichroic ratios as high as 4:1 for TiS_3[3] and 2.55:1 for ZrS_3,[4] and the dichroic ratio has been reported to depend on both the excitation energy[3−5] and the sample thickness.[4,6] Although established experimentally, the underlying mechanisms at play in this photocurrent production have not been intensely studied. Here, we show that these effects are the result of electronic orbital symmetry by comparing polarization-dependent scanning photocurrent microscopy (SPCM), along wires 45−85 nm in height by 0.5−0.9 μm wide, to polarization-dependent nanospot angle-resolved photoemission spectroscopy (nano-ARPES) for both TiS_3(001) and ZrS_3(001).

EXPERIMENTAL DETAILS

Nanowhiskers of TiS_3 and ZrS_3 were synthesized through direct reactions of metallic titanium or zirconium with sulfur vapor in vacuum-sealed quartz ampules, as described elsewhere.[1,2,7,10,12,16,37,38] Figure S1 in the Supporting Information shows optical photographs of TiS_3 and ZrS_3 crystals, as well as their Raman spectra. These spectra are in perfect agreement with the previously published reports[7,37,38] and confirm the high crystallinity of the TiS_3 and ZrS_3 whiskers. Phototransistors were fabricated by mechanically exfoliating TiS_3 and ZrS_3 crystals onto SiO_2 substrates, with the transistor channel parallel to the crystallographic $\vec{b}$ axis. Contacts 2 μm wide and ∼3 μm apart were defined using a Heidelberg BWL 66FS laser lithography system;

Received: June 30, 2020
Accepted: August 13, 2020
Published: August 13, 2020

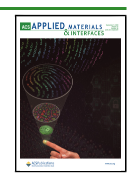

https://dx.doi.org/10.1021/acsami.0c11892
ACS Appl. Mater. Interfaces 2020, 12, 40525−40531

then, 5 nm of Cr and 45 nm of Au were deposited with an AJA electron-beam evaporation system, as indicated in Figure 1. *I*−*V*

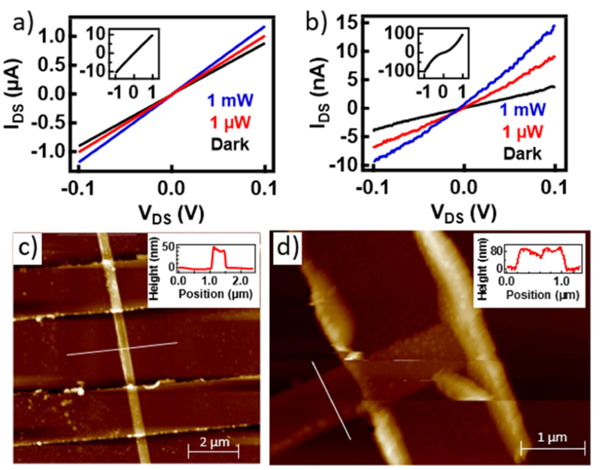

Figure 1. *I*−*V* curves for the (a) TiS_3 and (b) ZrS_3 phototransistors under different illumination intensities. The insets show expanded ranges to emphasize the difference in linearity. AFM of the (c) TiS_3 and (d) ZrS_3 phototransistors with insets showing the height profiles taken along the white lines.

curves indicate that this process forms largely Ohmic contacts on TiS_3 (Figure 1a), which is consistent with previous studies;[9,10,12] however, the contacts appear to form Schottky barriers on ZrS_3 (Figure 1b). It has been shown that pure Au forms superior contacts with TiS_3 because of strong bonding with the surface sulfur.[9] Au contacts may also reduce Schottky barrier formation in ZrS_3,[9,12] nonetheless, Au is a large work function metal and ZrS_3 is an n-type semiconductor, so Schottky barrier formation is generally expected. A recognized cause of low mobility in these systems is phonon scattering,[12] which appears to be suppressed by an overcoat of Al_2O_3.[10]

Both TiS_3 and ZrS_3 phototransistors show a considerable change in resistance under illumination, as shown in Figure 1, consistent with previous studies,[14,21] but this effect is reduced at higher voltages for ZrS_3 because of the nonlinearity of the *I*−*V* curves. Atomic force microscopy (AFM) was performed using a Bruker dimension ICON system, which shows that the TiS_3 phototransistor channel was roughly 45 nm tall and 500 nm wide (Figure 1c) and the ZrS_3 channel was approximately 85 nm tall and 900 nm wide (Figure 1d).

SPCM was performed with a 488 nm solid-state laser (Coherent Sapphire 100) passed through a neutral density filter followed by a linear polarizer, before being reflected off a dichroic mirror and focused onto the phototransistors using an inverted Olympus IX 81 microscope. The neutral density filter was used to maintain a light intensity of 100 μW for all measurements. Measurements were performed at normal incidence, so that the incident light was polarized perpendicular to the $\vec{c}$ axis. For more information on the SPCM setup, see the studies by Li et al.[39] and Chen et al.[40]

NanoARPES measurements were performed on the ANTARES beamline at the synchrotron SOLEIL[41] on nanowhiskers of TiS_3(001) and ZrS_3(001) that were exfoliated *in situ* under vacuum better than 10^{-10} Torr. Precise alignment and positioning on the nanowhiskers were achieved with a spot size of ∼500 nm.[1,2,42,43] Measurements were taken at an incidence angle of 45° with respect to the surface normal. The polarization dependence of nanoARPES was observed by comparing measurements where the plane of incidence coincides with either $\vec{a}-\vec{c}$ or $\vec{b}-\vec{c}$ crystallographic planes.

Thus far, all directions have been in terms of the crystallographic coordinate system; however, throughout this paper, we will also discuss the directions along the surface Brillouin zone (BZ) as well as the rectangular representation of the electron orbitals. It is convenient to clarify before going further that the quasi-1D chains lie along the crystallographic $\vec{b}$ axis, which corresponds to the $\vec{y}$ axis of the electron orbitals and the $\bar{\Gamma}$ to $\bar{Y}$ direction along the BZ. Similarly, the crystallographic $\vec{a}$ axis maps to the $\vec{x}$ electron orbital axis and the $\bar{\Gamma}$ to $\bar{B}$ direction of the BZ. To avoid confusion, the BZ directions will always be noted as either $\bar{\Gamma}$ to $\bar{Y}$ or $\bar{\Gamma}$ to $\bar{B}$.

■ RESULTS AND DISCUSSION

The SPCM images of TiS_3(001) and ZrS_3(001) are shown in Figure 2 with an excitation energy of 2.5 eV (488 nm) and the incident light polarized along either the $\vec{b}$ ($\theta = 0°$) or $\vec{a}$ ($\theta = 90°$) axis. For both materials, the photocurrent intensity shows a notable polarization dependence, which is consistent with other polarization studies on TiS_3(001)[3,5,6,35,36] and ZrS_3(001).[4,6,20] However, the change in photocurrent intensity as a result of changing light polarization is far more significant for ZrS_3(001) than for TiS_3(001), as seen by the photocurrent images in Figure 2, where the dichroic ratio for ZrS_3(001) is ∼4:1, but for TiS_3(001), the ratio is only ∼1.2:1.

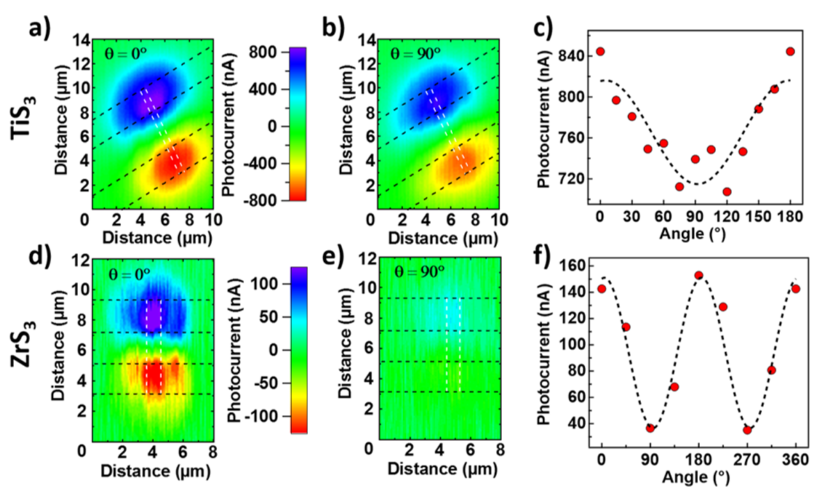

Figure 2. SPCM images of TiS_3(001) (a,b) and ZrS_3(001) (d,e) using light polarized along the $\vec{b}$ (a,d) and $\vec{a}$ (b,e) axes. The dotted black and white lines indicate the contacts and transistor channel, respectively. Angle dependence of the photocurrent intensity in TiS_3 (c) and ZrS_3 (f), where the angle is measured with respect to the *b*-axis. The photocurrent intensities in (c) and (f) are the average of the photocurrent magnitudes at the source and drain.

https://dx.doi.org/10.1021/acsami.0c11892
ACS Appl. Mater. Interfaces 2020, 12, 40525−40531

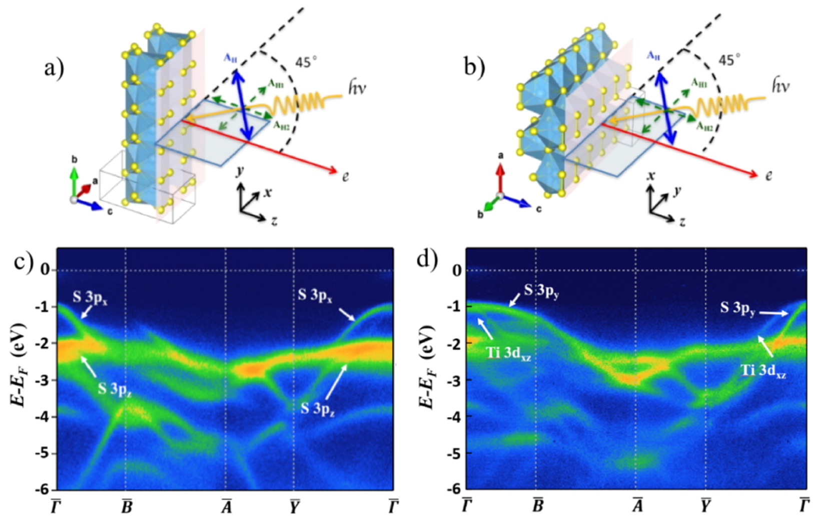

Figure 3. Experimental setups illustrating polarizations (a) $\varepsilon_x + \varepsilon_z$ and (b) $\varepsilon_z + \varepsilon_y$ used in the ARPES measurements of $TiS_3(001)$ shown in (c,d), respectively, taken at a photon energy of 100 eV.

The polarization-dependent behavior can be explained by examining the average electron transition rate dictated by Fermi's golden rule,[44−50] which is shown in eq 1

$$\Gamma = \frac{2\pi}{\hbar} |\langle \varphi_f | H' | \varphi_i \rangle|^2 \delta(E_f - E_i - \hbar\omega) \quad (1)$$

where φ_i, φ_f, E_i, and E_f are the initial and final state wave functions and energies, respectively, and H' is the perturbation Hamiltonian. For photoexcitation measurements, H' can be approximated as $\frac{e}{m_e c}\vec{A}\cdot\vec{P}$ where $\vec{A}$ is the vector potential and $\vec{P}$ is the momentum operator, under the assumptions that the field is sufficiently weak so that $|\vec{A}|^2$ is negligible and the momentum of the photon is negligible compared to the electron's momentum.[49,50] Using this approximation, $H'|\varphi_i\rangle$ is proportional to $\vec{\varepsilon}\cdot\vec{r}$ where $\vec{\varepsilon}$ is the light polarization vector and $\vec{r}$ is the dipole of the electron orbital. Furthermore, group theory considerations dictate that the transition will only occur if $\vec{\varepsilon}\cdot\vec{r}$ belongs to the same irreducible representation as φ_f. The TMTs belong to the $P2_1/m$ space group[1,2,51] where the rotation axis is along the crystallographic b axis. This space group corresponds to the C_{2h} group symmetry in Schönflies notation. However, at the surface of the material, both rotational and inversion symmetries are lost such that the group symmetry reduces to C_s. This loss of symmetry and the corresponding change in the selection rules are likely responsible for the dependence of the dichroic ratio on the sample thickness.[4,6] Based on density functional theory (DFT) calculations,[52] the bottom of the conduction band in TiS_3 is dominated by the Ti $3d_{z^2}$ and $3d_{x^2-y^2}$ electron orbitals. Similarly, the bottom of the conduction band in ZrS_3 should be largely Zr $4d_{z^2}$ and $4d_{x^2-y^2}$.[53] All of these orbitals belong to the highest symmetry irreducible representations in the C_{2h} and C_s symmetry groups. If the final states are limited to d_{z^2} and $d_{x^2-y^2}$, then, in the bulk with C_{2h} symmetry, light polarized along the orbital y axis (ε_y = along the chains) will exclusively excite electrons from the p_y orbitals and light polarized along the x axis (ε_x) will excite the p_x orbitals. Because of the reduction of symmetry at the surface, ε_y can also excite the d_{yz} and d_{xy} orbitals and $\varepsilon_x + \varepsilon_z$ can also excite the d_{xz}, d_{z^2}, and $d_{x^2-y^2}$ orbitals, though the latter two should have negligible contributions to the valence band.[52,53] These additional excitations will only occur if there is p−d hybridization since d → d transitions are optically forbidden.[49,50] The stronger photocurrent signal using ε_y (Figure 2) indicates that the p_y orbitals contribute most strongly to photocurrent production.

The cause of the p_y dominance, in the dichroism of photoconductance, can be examined through symmetry assignments of the experimentally determined band structure using polarization-dependent nanoARPES, which is shown for $TiS_3(001)$ and $ZrS_3(001)$ in Figures 3 and 4, respectively.

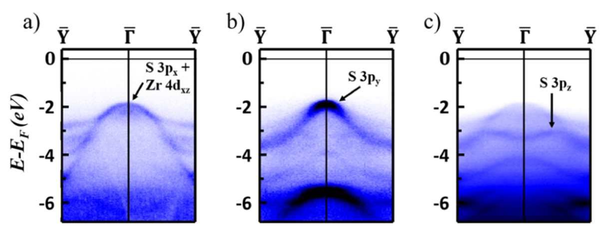

Figure 4. Angle-resolved photoemission derived band structure of $ZrS_3(001)$ using incident light polarizations (a) ε_x, (b) ε_y, and (c) $\varepsilon_x + \varepsilon_z$. The photon energy is 130 eV.

Photoemission is extremely surface sensitive with a final state that is a fully symmetric free electron such that the selection rules are the same as the photocurrent measurements. Electron orbitals within the same irreducible representations were distinguished with the assistance of previously reported DFT calculations.[52,53]

Figure 3a schematically shows the light polarization geometry for the nanoARPES measurements on $TiS_3(001)$ shown in Figure 3c where $\vec{\varepsilon} = \varepsilon_x + \varepsilon_z$. Our previous work[1,2] utilized this polarization because it emphasizes the top of the valence band, which may be attributed to the S $3p_x$ orbitals.[52,53] These p_x orbitals are highly anisotropic with a hole effective mass that is twice as large along $\bar{\Gamma}$ to $\bar{Y}$ than along $\bar{\Gamma}$ to $\bar{B}$, as has been noted elsewhere.[1,2] The S $3p_z$ orbitals contribute most strongly to the band structure 2 eV below the Fermi level (E_F) or ∼1 eV below the valence band maximum, and these bands have minimal dispersion. The S $3p_z$ weighted bands are very evident with light polarized along $\varepsilon_x + \varepsilon_z$ (Figure 3c), and the symmetry selection rules allow photoemission from this initial state. The features of the S $3p_z$ bands

https://dx.doi.org/10.1021/acsami.0c11892
ACS Appl. Mater. Interfaces 2020, 12, 40525−40531

can be more easily discerned after a second derivative treatment of the data, which was reported in our previous work.[2] Both of these assignments are in agreement with DFT calculations.[52]

When the light polarization is switched to $\vec{\varepsilon} = \varepsilon_z + \varepsilon_y$ (Figure 3b), additional bands are observed near the top of the valence band (Figure 3d) which can be assigned to the S $3p_y$ orbitals. The S $3p_x$ and $3p_y$ orbitals at the top of the valence band are nearly degenerate at $\bar{\Gamma}$, contrary to DFT calculations, which place the $3p_y$ orbital weighted band at a binding energy well below the $3p_x$ orbital.[3,20,52−54] Unlike the $3p_x$ orbitals, the $3p_y$ bands have a significantly larger hole effective mass along $\bar{\Gamma}$ to $\bar{B}$ than along $\bar{\Gamma}$ to $\bar{Y}$. The $3p_x$ hybridized bands remain visible, though significantly weaker, with the light polarization perpendicular to the $\vec{x}$ orbital axis. This indicates that although these bands are mostly S $3p_x$ weighted, they also have other contributions which DFT calculations[52] place as largely the Ti $3d_{xz}$ orbitals.

The nanoARPES measurements on $ZrS_3(001)$ with polarization vectors ε_x, ε_y, and $\varepsilon_x + \varepsilon_z$ are shown in Figure 4a−c, respectively. As with $TiS_3(001)$, the S $3p_x$ and $3p_y$ orbitals in $ZrS_3(001)$ are both present near the top of the valence band and nearly degenerate at $\bar{\Gamma}$. Previous ARPES measurements on $ZrS_3(001)$ attributed these two bands to spin−orbit coupling.[55] The orbital symmetries of these two bands, near the top of the valence band, are observed to be significantly different in Figure 4. Furthermore, the spectral weight assignments to sulfur weight p bands, as suggested by theory, and the absence of wave vector displacement that is typical of spin−orbit coupling indicate that this band splitting at the top of the valence band at $\bar{\Gamma}$ is not dominated by spin−orbit splitting and has no exchange splitting contribution.

The S $3p_x$ orbital weighted band is almost entirely absent in Figure 4c which is consistent with S $3p_x$ combined with a minor Zr $4d_{xz}$ component dominating the top of the valence band. As with TiS_3, the S $3p_z$ character states in ZrS_3 contribute to the valence band structure at binding energies ∼1 eV below the valence band maximum. These symmetry assignments are the same as seen in Figure 3 for $TiS_3(001)$ and agree with DFT for $TiS_3(001)$[52] and $ZrS_3(001)$.[53]

Based on Figures 3 and 4, the S p_y orbitals extend from close to the valence band maximum to binding energies ∼2 eV below the valence band maximum. The S p_y orbitals, nonetheless, have a strong spectral weight density within 0.5 eV of the valence band maximum. Because the top of the valence band occurs at the center of the BZ,[1,2] the near degeneracy of the p_y and p_x bands at the center of the BZ, $\bar{\Gamma}$, affects light polarization sensitivity. If the trichalcogenide S p_x orbital weighted band occurred at significantly higher binding energies than the S p_y orbital weight bands, as suggested by theory,[3,20,52−54] then excitation energies close to the band gap would generate larger photocurrents with light polarized perpendicular to the 1D chains, resulting in a region of photon energy where the dichroic ratio could switch.

Larger Z value TMTs, specifically $ZrSe_3$ and $HfSe_3$, do exhibit an appreciable splitting in binding energy between the trichalcogenide S p_x and S p_y bands at $\bar{\Gamma}$,[55] but this splitting is not resolved here at $\bar{\Gamma}$, the center of the surface BZ, for $TiS_3(001)$ and $ZrS_3(001)$, as seen in Figures 3 and 4, respectively. Yet, the existing band structure calculations,[52,53] that include symmetry assignments, are seen to be in agreement with the experiment. The band structure is also seen to be consistent with many of the device characteristics as noted elsewhere.[12]

Since the d_{z^2} and $d_{x^2-y^2}$ orbitals dominate the bottom 0.5 eV of the conduction band for both ZrS_3 and TiS_3,[52,53] it is expected that the dichroic ratios will be maximized with excitation energies within 1 eV of the band gap and will begin to diminish for larger excitation energies. The band gaps for TiS_3 and ZrS_3 are ∼1[2,14,15,17,54,56,57] and ∼2 eV,[1,4,20,53,54,58−61] respectively, so that the dichroic ratios should be maximized with excitation energies of 1.0−2.0 eV for TiS_3 and 2.0−3.0 eV for ZrS_3. This conclusion is supported by comparison of the presently reported SPCM data with other experimental measurements.[3−6] Here, the polarization dependence of the photoconductance is far more significant for $ZrS_3(001)$ than for $TiS_3(001)$, but the photon energy of 2.5 eV (488 nm) used here is much closer to the band gap of ZrS_3 than TiS_3. For TiS_3, the dichroic ratio has been observed to increase as the photon excitation energy is decreased from 2.3 to 1.5 eV.[3] Although prior absorption calculations vary significantly,[3−5,62] they tend to place the maximum dichroic ratio at slightly higher excitation energies, which is likely caused by the discrepancies between calculated[3,20,52−54] and experimental[1,2,55] band structures mentioned earlier. Indeed, the optical excitation wavelength used here (488 nm) is very close to the observed optical resonance seen for $ZrS_3(001)$ (see Figure S2 in the Supporting Information). Despite possible discrepancies, it is clear that when combined, TiS_3 and ZrS_3 have promise as polarization sensitive photodetectors over a wide range of wavelengths.

■ CONCLUSIONS

Both $TiS_3(001)$ and $ZrS_3(001)$ exhibit strongly polarization sensitive photocurrent production because of their electronic bands with distinct in-plane symmetries. As we have noted, existing band structure calculations that include symmetry assignments, as noted elsewhere,[52,53] are seen to be in agreement with the experiment. The S $3p_y$ orbital weighted band is strongest within 0.5 eV of valence band maximum and dominates photocurrent production. Because the bottom 0.5 eV of the conduction band for both materials is comprised primarily of d_{z^2} and $d_{x^2-y^2}$ orbitals, the dichroism in the photocurrent production will be most significant for excitation energies between 1.0 and 2.0 eV for $TiS_3(001)$ and 2.0 and 3.0 eV for $ZrS_3(001)$. Thus, TiS_3 and ZrS_3 show considerable promise as versatile polarization sensitive photodetectors across the visible spectrum and into the near-infrared.

■ ASSOCIATED CONTENT

Supporting Information

The Supporting Information is available free of charge at https://pubs.acs.org/doi/10.1021/acsami.0c11892.

Raman spectra and optical absorption spectra of suspensions of TiS_3 and ZrS_3 (PDF)

■ AUTHOR INFORMATION

Corresponding Author

Peter A. Dowben − *Department of Physics and Astronomy, University of Nebraska-Lincoln, Lincoln, Nebraska 68588-0299, United States;* orcid.org/0000-0002-2198-4710; Phone: 402-472-9838; Email: pdowben1@unl.edu; Fax: 402-472-6148.

https://dx.doi.org/10.1021/acsami.0c11892
ACS Appl. Mater. Interfaces 2020, 12, 40525−40531

Authors

Simeon J. Gilbert − *Department of Physics and Astronomy, University of Nebraska-Lincoln, Lincoln, Nebraska 68588-0299, United States*

Hemian Yi − *Synchrotron SOLEIL and Université Paris-Saclay, 91190 Saint-Aubin, France*

Jia-Shiang Chen − *Center for Functional Nanomaterials, Brookhaven National Laboratory, 11973 Upton, New York, United States;* orcid.org/0000-0003-1612-3008

Andrew J. Yost − *Department of Physics, Oklahoma State University, Stillwater, Oklahoma 74078-3072, United States;* orcid.org/0000-0002-6220-7520

Archit Dhingra − *Department of Physics and Astronomy, University of Nebraska-Lincoln, Lincoln, Nebraska 68588-0299, United States*

Jehad Abourahma − *Department of Chemistry, University of Nebraska-Lincoln, Lincoln, Nebraska 68588-0304, United States*

Alexey Lipatov − *Department of Chemistry, University of Nebraska-Lincoln, Lincoln, Nebraska 68588-0304, United States;* orcid.org/0000-0001-5043-1616

Jose Avila − *Synchrotron SOLEIL and Université Paris-Saclay, 91190 Saint-Aubin, France*

Takashi Komesu − *Department of Physics and Astronomy, University of Nebraska-Lincoln, Lincoln, Nebraska 68588-0299, United States*

Alexander Sinitskii − *Department of Chemistry, University of Nebraska-Lincoln, Lincoln, Nebraska 68588-0304, United States;* orcid.org/0000-0002-8688-3451

Maria C. Asensio − *Materials Science Institute of Madrid (ICMM), Spanish Scientific Research Council (CSIC), Valencia Institute of Materials Science (ICMUV), MATINEE: CSIC Associated Unit-ICMM-ICMUV Valencia University, E-28049 Madrid, Spain;* orcid.org/0000-0001-8252-7655

Complete contact information is available at: https://pubs.acs.org/10.1021/acsami.0c11892

Author Contributions

P.A.D., A.J.Y., M.C.A., and S.J.G. developed the experimental concepts. H.Y., Jose Avila, and M.C.A. conducted the nanoARPES measurements. H.Y., Jose Avila, M.C.A., S.J.G., and T.K. analyzed the corresponding nanoARPES data. S.J.G., J.-S.C., and A.D. conducted the SPCM and $I-V$ measurements and analyzed the corresponding data. S.J.G. fabricated the transistor devices and performed AFM. A.L., Jehad Abourahma, and A.S. grew and characterized the TiS_3 and ZrS_3 crystals. The conclusions were formed through discussions by all authors. The manuscript was written by S.J.G. and P.A.D. with contributions and suggestions from all authors.

Notes

The authors declare no competing financial interest.

■ ACKNOWLEDGMENTS

This research was supported by the National Science Foundation through grant NSF-ECCS 1740136, as well as by the nCORE, a wholly owned subsidiary of the Semiconductor Research Corporation (SRC), through the Center on Antiferromagnetic Magneto-electric Memory and Logic task #2760.002. The Synchrotron SOLEIL is supported by the Centre National de la Recherche Scientifique (CNRS) and the Commissariat à l'Energie Atomique et aux Energies Alternatives (CEA), France. This work was also supported by a public grant by the French National Research Agency (ANR) as part of the "Investissements d'Avenir" (reference: ANR-17-CE09-0016-05). The research was performed in part in the Nebraska Nanoscale Facility: National Nanotechnology Coordinated Infrastructure and the Nebraska Center for Materials and Nanoscience, which are supported by the National Science Foundation under Award ECCS: 1542182, and the Nebraska Research Initiative. This research used resources of the Center for Functional Nanomaterials, which is a U.S. DOE Office of Science Facility at Brookhaven National Laboratory under contract no. DE-SC0012704.

■ REFERENCES

(1) Yi, H.; Gilbert, S. J.; Lipatov, A.; Sinitskii, A.; Avila, J.; Abourahma, J.; Komesu, T.; Asensio, M. C.; Dowben, P. A. The Electronic Band Structure of Quasi-One-Dimensional van Der Waals Semiconductors: The Effective Hole Mass of ZrS_3 Compared to TiS_3. *J. Phys.: Condens. Matter* **2020**, *32*, 29LT01.

(2) Yi, H.; Komesu, T.; Gilbert, S.; Hao, G.; Yost, A. J.; Lipatov, A.; Sinitskii, A.; Avila, J.; Chen, C.; Asensio, M. C.; Dowben, P. A. The Band Structure of the Quasi-One-Dimensional Layered Semiconductor TiS_3(001). *Appl. Phys. Lett.* **2018**, *112*, 052102.

(3) Liu, S.; Xiao, W.; Zhong, M.; Pan, L.; Wang, X.; Deng, H.-X.; Liu, J.; Li, J.; Wei, Z. Highly Polarization Sensitive Photodetectors Based on Quasi-1D Titanium Trisulfide (TiS_3). *Nanotechnology* **2018**, *29*, 184002.

(4) Wang, X.; Wu, K.; Blei, M.; Wang, Y.; Pan, L.; Zhao, K.; Shan, C.; Lei, M.; Cui, Y.; Chen, B.; Wright, D.; Hu, W.; Tongay, S.; Wei, Z. Highly Polarized Photoelectrical Response in VdW ZrS_3 Nanoribbons. *Adv. Electron. Mater.* **2019**, *5*, 1900419.

(5) Island, J. O.; Biele, R.; Barawi, M.; Clamagirand, J. M.; Ares, J. R.; Sánchez, C.; van Der Zant, H. S. J.; Ferrer, I. J.; D'Agosta, R.; Castellanos-Gomez, A. Titanium Trisulfide (TiS_3): A 2D Semiconductor with Quasi-1D Optical and Electronic Properties. *Sci. Rep.* **2016**, *6*, 22214.

(6) Kong, W.; Bacaksiz, C.; Chen, B.; Wu, K.; Blei, M.; Fan, X.; Shen, Y.; Sahin, H.; Wright, D.; Narang, D. S.; Tongay, S. Angle Resolved Vibrational Properties of Anisotropic Transition Metal Trichalcogenide Nanosheets. *Nanoscale* **2017**, *9*, 4175−4182.

(7) Lipatov, A.; Loes, M. J.; Lu, H.; Dai, J.; Patoka, P.; Vorobeva, N. S.; Muratov, D. S.; Ulrich, G.; Kästner, B.; Hoehl, A.; Ulm, G.; Zeng, X. C.; Rühl, E.; Gruverman, A.; Dowben, P. A.; Sinitskii, A. Quasi-1D TiS_3 Nanoribbons: Mechanical Exfoliation and Thickness-Dependent Raman Spectroscopy. *ACS Nano* **2018**, *12*, 12713−12720.

(8) Island, J. O.; Barawi, M.; Biele, R.; Almazán, A.; Clamagirand, J. M.; Ares, J. R.; Sánchez, C.; van Der Zant, H. S. J.; Álvarez, J. V.; D'Agosta, R.; Ferrer, I. J.; Castellanos-Gomez, A. TiS_3 Transistors with Tailored Morphology and Electrical Properties. *Adv. Mater.* **2015**, *27*, 2595−2601.

(9) Gilbert, S. J.; Lipatov, A.; Yost, A. J.; Loes, M. J.; Sinitskii, A.; Dowben, P. A. The Electronic Properties of Au and Pt Metal Contacts on Quasi-One-Dimensional Layered TiS_3(001). *Appl. Phys. Lett.* **2019**, *114*, 101604.

(10) Lipatov, A.; Wilson, P. M.; Shekhirev, M.; Teeter, J. D.; Netusil, R.; Sinitskii, A. Few-Layered Titanium Trisulfide (TiS_3) Field-Effect Transistors. *Nanoscale* **2015**, *7*, 12291−12296.

(11) Molina-Mendoza, A. J.; Island, J. O.; Paz, W. S.; Clamagirand, J. M.; Ares, J. R.; Flores, E.; Leardini, F.; Sánchez, C.; Agraït, N.; Rubio-Bollinger, G.; van der Zant, H. S. J.; Ferrer, I. J.; Palacios, J. J.; Castellanos-Gomez, A. High Current Density Electrical Breakdown of TiS_3 Nanoribbon-Based Field-Effect Transistors. *Adv. Funct. Mater.* **2017**, *27*, 1605647.

(12) Randle, M.; Lipatov, A.; Kumar, A.; Kwan, C.-P.; Nathawat, J.; Barut, B.; Yin, S.; He, K.; Arabchigavkani, N.; Dixit, R.; Komesu, T.; Avila, J.; Asensio, M. C.; Dowben, P. A.; Sinitskii, A.; Singisetti, U.; Bird, J. P. Gate-Controlled Metal−Insulator Transition in TiS_3 Nanowire Field-Effect Transistors. *ACS Nano* **2018**, *13*, 803−811.

(13) Xiong, W.-W.; Chen, J.-Q.; Wu, X.-C.; Zhu, J.-J. Individual HfS_3 Nanobelt for Field-Effect Transistor and High Performance Visible-Light Detector. *J. Mater. Chem. C* **2014**, *2*, 7392.

(14) Island, J. O.; Buscema, M.; Barawi, M.; Clamagirand, J. M.; Ares, J. R.; Sánchez, C.; Ferrer, I. J.; Steele, G. A.; van der Zant, H. S. J.; Castellanos-Gomez, A. Ultrahigh Photoresponse of Few-Layer TiS_3 Nanoribbon Transistors. *Adv. Opt. Mater.* **2014**, *2*, 641−645.

(15) Ferrer, I. J.; Maciá, M. D.; Carcelén, V.; Ares, J. R.; Sánchez, C. On the Photoelectrochemical Properties of TiS_3 Films. *Energy Procedia* **2012**, *22*, 48−52.

(16) Cui, Q.; Lipatov, A.; Wilt, J. S.; Bellus, M. Z.; Zeng, X. C.; Wu, J.; Sinitskii, A.; Zhao, H. Time-Resolved Measurements of Photocarrier Dynamics in TiS_3 Nanoribbons. *ACS Appl. Mater. Interfaces* **2016**, *8*, 18334−18338.

(17) Ferrer, I. J.; Ares, J. R.; Clamagirand, J. M.; Barawi, M.; Sánchez, C. Optical Properties of Titanium Trisulphide (TiS_3) Thin Films. *Thin Solid Films* **2013**, *535*, 398−401.

(18) Niu, Y.; Frisenda, R.; Flores, E.; Ares, J. R.; Jiao, W.; Perez de Lara, D.; Sánchez, C.; Wang, R.; Ferrer, I. J.; Castellanos-Gomez, A. Polarization-Sensitive and Broadband Photodetection Based on a Mixed-Dimensionality TiS_3/Si p-n Junction. *Adv. Opt. Mater.* **2018**, *6*, 1800351.

(19) Talib, M.; Tabassum, R.; Abid; Islam, S. S.; Mishra, P. Improvements in the Performance of a Visible−NIR Photodetector Using Horizontally Aligned TiS_3 Nanoribbons. *ACS Omega* **2019**, *4*, 6180−6191.

(20) Pant, A.; Torun, E.; Chen, B.; Bhat, S.; Fan, X.; Wu, K.; Wright, D. P.; Peeters, F. M.; Soignard, E.; Sahin, H.; Tongay, S. Strong Dichroic Emission in the Pseudo One Dimensional Material ZrS_3. *Nanoscale* **2016**, *8*, 16259−16265.

(21) Tao, Y.-R.; Wu, J.-J.; Wu, X.-C. Enhanced Ultraviolet-Visible Light Responses of Phototransistors Based on Single and a Few ZrS_3 Nanobelts. *Nanoscale* **2015**, *7*, 14292−14298.

(22) Yang, S.; Wu, M.; Shen, W.; Huang, L.; Tongay, S.; Wu, K.; Wei, B.; Qin, Y.; Wang, Z.; Jiang, C.; Hu, C. Highly Sensitive Polarization Photodetection Using a Pseudo-One-Dimensional $Nb_{(1-x)}Ti_xS_3$ Alloy. *ACS Appl. Mater. Interfaces* **2019**, *11*, 3342−3352.

(23) Morozova, N. V.; Korobeinikov, I. V.; Kurochka, K. V.; Titov, A. N.; Ovsyannikov, S. V. Thermoelectric Properties of Compressed Titanium and Zirconium Trichalcogenides. *J. Phys. Chem. C* **2018**, *122*, 14362−14372.

(24) Sakuma, T.; Nishino, S.; Miyata, M.; Koyano, M. Thermoelectric Properties for a Suspended Microribbon of Quasi-One-Dimensional TiS_3. *J. Electron. Mater.* **2018**, *47*, 3177−3183.

(25) Guilmeau, E.; Berthebaud, D.; Misse, P. R. N.; Hébert, S.; Lebedev, O. I.; Chateigner, D.; Martin, C.; Maignan, A. $ZrSe_3$-Type Variant of TiS_3: Structure and Thermoelectric Properties. *Chem. Mater.* **2014**, *26*, 5585−5591.

(26) Zhang, J.; Liu, X.; Wen, Y.; Shi, L.; Chen, R.; Liu, H.; Shan, B. Titanium Trisulfide Monolayer as a Potential Thermoelectric Material: A First-Principles-Based Boltzmann Transport Study. *ACS Appl. Mater. Interfaces* **2017**, *9*, 2509−2515.

(27) Tanibata, N.; Matsuyama, T.; Hayashi, A.; Tatsumisago, M. All-Solid-State Sodium Batteries Using Amorphous TiS_3 Electrode with High Capacity. *J. Power Sources* **2015**, *275*, 284−287.

(28) Liu, Y.; Lian, J.; Yang, X. Rechargeable Mg Battery Cathode TiS_3 with d-p Orbital Hybridized Electronic Structures Related Content First-Principles Calculation for Point Defects in $Li_2Ti_2O_4$. *Appl. Phys. Express* **2016**, *9*, 011801.

(29) Arsentev, M.; Missyul, A.; Petrov, A. V.; Hammouri, M. TiS_3 Magnesium Battery Material: Atomic-Scale Study of Maximum Capacity and Structural Behavior. *J. Phys. Chem. C* **2017**, *121*, 15509−15515.

(30) Wu, J.; Wang, D.; Liu, H.; Lau, W.-M.; Liu, L.-M. An Ab Initio Study of TiS_3: A Promising Electrode Material for Rechargeable Li and Na Ion Batteries. *RSC Adv.* **2015**, *5*, 21455−21463.

(31) Empante, T. A.; Martinez, A.; Wurch, M.; Zhu, Y.; Geremew, A. K.; Yamaguchi, K.; Isarraraz, M.; Rumyantsev, S.; Reed, E. J.; Balandin, A. A.; Bartels, L. Low Resistivity and High Breakdown Current Density of 10 nm Diameter van der Waals $TaSe_3$ Nanowires by Chemical Vapor Deposition. *Nano Lett.* **2019**, *19*, 4355−4361.

(32) Geremew, A.; Bloodgood, M. A.; Aytan, E.; Woo, B. W. K.; Corber, S. R.; Liu, G.; Bozhilov, K.; Salguero, T. T.; Rumyantsev, S.; Rao, M. P.; Balandin, A. A. Current Carrying Capacity of Quasi-1D $ZrTe_3$ van Der Waals Nanoribbons. *IEEE Electron Device Lett.* **2018**, *39*, 735−738.

(33) Liu, G.; Rumyantsev, S.; Bloodgood, M. A.; Salguero, T. T.; Shur, M.; Balandin, A. A. Low-Frequency Electronic Noise in Quasi-1D $TaSe_3$ van der Waals Nanowires. *Nano Lett.* **2017**, *17*, 377−383.

(34) Stolyarov, M. A.; Liu, G.; Bloodgood, M. A.; Aytan, E.; Jiang, C.; Samnakay, R.; Salguero, T. T.; Nika, D. L.; Rumyantsev, S. L.; Shur, M. S.; Bozhilov, K. N.; Balandin, A. A. Breakdown current density in h-BN-capped quasi-1D $TaSe_3$ metallic nanowires: prospects of interconnect applications. *Nanoscale* **2016**, *8*, 15774−15782.

(35) Khatibi, A.; Godiksen, R. H.; Basuvalingam, S. B.; Pellegrino, D.; Bol, A. A.; Shokri, B.; Curto, A. G. Anisotropic Infrared Light Emission from Quasi-1D Layered TiS_3. *2D Mater.* **2019**, *7*, 015022.

(36) Papadopoulos, N.; Frisenda, R.; Biele, R.; Flores, E.; Ares, J. R.; Sánchez, C.; van der Zant, H. S. J.; Ferrer, I. J.; D'Agosta, R.; Castellanos-Gomez, A. Large Birefringence and Linear Dichroism in TiS_3 Nanosheets. *Nanoscale* **2018**, *10*, 12424−12429.

(37) Muratov, D. S.; Ishteev, A. R.; Lypenko, D. A.; Vanyushin, V. O.; Gostishev, P.; Perova, S.; Saranin, D. S.; Rossi, D.; Auf Der Maur, M.; Volonakis, G.; Giustino, F.; Persson, P. O. Å.; Kuznetsov, D. V.; Sinitskii, A.; Di Carlo, A. Slot-Die-Printed Two-Dimensional ZrS_3 Charge Transport Layer for Perovskite Light-Emitting Diodes. *ACS Appl. Mater. Interfaces* **2019**, *11*, 48021−48028.

(38) Muratov, D. S.; Vanyushin, V. O.; Vorobeva, N. S.; Jukova, P.; Lipatov, A.; Kolesnikov, E. A.; Karpenkov, D.; Kuznetsov, D. V.; Sinitskii, A. Synthesis and Exfoliation of Quasi-1D $(Zr,Ti)S_3$ Solid Solutions for Device Measurements. *J. Alloys Compd.* **2020**, *815*, 152316.

(39) Li, M.; Chen, J.-S.; Routh, P. K.; Zahl, P.; Nam, C.-Y.; Cotlet, M. Distinct Optoelectronic Signatures for Charge Transfer and Energy Transfer in Quantum Dot-MoS_2 Hybrid Photodetectors Revealed by Photocurrent Imaging Microscopy. *Adv. Funct. Mater.* **2018**, *28*, 1707558.

(40) Chen, J.-S.; Li, M.; Wu, Q.; Fron, E.; Tong, X.; Cotlet, M. Layer-Dependent Photoinduced Electron Transfer in 0D-2D Lead Sulfide/Cadmium Sulfide-Layered Molybdenum Disulfide Hybrids. *ACS Nano* **2019**, *13*, 8461−8468.

(41) Avila, J.; Razado-Colambo, I.; Lorcy, S.; Lagarde, B.; Giorgetta, J.-L.; Polack, F.; Asensio, M. C. ANTARES, a Scanning Photoemission Microscopy Beamline at SOLEIL. *J. Phys.: Conf. Ser.* **2013**, *425*, 192023.

(42) Avila, J.; Razado, I.; Lorcy, S.; Fleurier, R.; Pichonat, E.; Vignaud, D.; Wallart, X.; Asensio, M. C. Exploring Electronic Structure of One-Atom Thick Polycrystalline Graphene Films: A Nano Angle Resolved Photoemission Study. *Sci. Rep.* **2013**, *3*, 2439.

(43) Avila, J.; Asensio, M. C. First NanoARPES User Facility Available at SOLEIL: An Innovative and Powerful Tool for Studying Advanced Materials. *Synchrotron Radiat. News* **2014**, *27*, 24−30.

(44) Feibelman, P. J.; Eastman, D. E. Photoemission spectroscopy-Correspondence between quantum theory and experimental phenomenology. *Phys. Rev. B: Condens. Matter Mater. Phys.* **1974**, *10*, 4932−4947.

(45) Mahan, G. D. Theory of Photoemission in Simple Metals. *Phys. Rev. B: Condens. Matter Mater. Phys.* **1970**, *2*, 4334−4350.

(46) Adawi, I. Theory of the Surface Photoelectric Effect for One and Two Photons. *Phys. Rev.* **1964**, *134*, A788−A798.

(47) Schaich, W. L.; Ashcroft, N. W. Model Calculations in the Theory of Photoemission. *Phys. Rev. B: Condens. Matter Mater. Phys.* **1971**, *3*, 2452−2465.

(48) Asensio, M. C.; Avila, J.; Roca, L.; Tejeda, A.; Gu, G. D.; Lindroos, M.; Markiewicz, R. S.; Bansil, A. Emergence of multiple Fermi surface maps in angle-resolved photoemission from $Bi_2Sr_2CaCu_2O_{8+\delta}$. *Phys. Rev. B: Condens. Matter Mater. Phys.* **2003**, *67*, 014519.

https://dx.doi.org/10.1021/acsami.0c11892
ACS Appl. Mater. Interfaces 2020, 12, 40525−40531

(49) Dowben, P. A.; Choi, J.; Morikawa, E.; Xu, B. The Band Structure and Orientation of Molecular Adsorbates on Surfaces by Angle-Resolved Electron Spectroscopies". In *Handbook of Thin Films*; Nalwa, H. S., Ed.; Characterization and Spectroscopy of Thin Films 2002; Academic Press, 2001; Chapter 2, Vol. 2, pp 61−114.
(50) Plummer, E. W.; Eberhardt, W. Angle-Resolved Photoemission as a Tool for the Study of Surfaces. *Adv. Chem. Phys.* **2007**, *49*, 533−656.
(51) Furuseth, S.; BrattÅs, L.; Kjekshus, A.; Fischer, P. On the Crystal Structures of TiS3, ZrS3, ZrSe3, ZrTe3, HfS3, and HfSe3. *Acta Chem. Scand.* **1975**, *29a*, 623−631.
(52) Silva-Guillén, J. A.; Canadell, E.; Ordejón, P.; Guinea, F.; Roldán, R. Anisotropic Features in the Electronic Structure of the Two-Dimensional Transition Metal Trichalcogenide TiS_3: Electron Doping and Plasmons. *2D Mater.* **2017**, *4*, 025085.
(53) Li, M.; Dai, J.; Zeng, X. C. Tuning the Electronic Properties of Transition-Metal Trichalcogenides via Tensile Strain. *Nanoscale* **2015**, *7*, 15385−15391.
(54) Jin, Y.; Li, X.; Yang, J. Single Layer of MX_3 (M = Ti, Zr; X = S, Se, Te): A New Platform for Nano-Electronics and Optics. *Phys. Chem. Chem. Phys.* **2015**, *17*, 18665−18669.
(55) Pacilé, D.; Papagno, M.; Lavagnini, M.; Berger, H.; Degiorgi, L.; Grioni, M. Photoemission and Optical Studies of $ZrSe_3$, $HfSe_3$, and ZrS_3. *Phys. Rev. B: Condens. Matter Mater. Phys.* **2007**, *76*, 155406.
(56) Dai, J.; Zeng, X. C. Titanium Trisulfide Monolayer: Theoretical Prediction of a New Direct-Gap Semiconductor with High and Anisotropic Carrier Mobility. *Angew. Chem., Int. Ed.* **2015**, *54*, 7572−7576.
(57) Molina-Mendoza, A. J.; Barawi, M.; Biele, R.; Flores, E.; Ares, J. R.; Sánchez, C.; Rubio-Bollinger, G.; Agraït, N.; D'Agosta, R.; Ferrer, I. J.; Castellanos-Gomez, A. Electronic Bandgap and Exciton Binding Energy of Layered Semiconductor TiS_3. *Adv. Electron. Mater.* **2015**, *1*, 1500126.
(58) Kurita, S.; Staehli, J. L.; Guzzi, M.; Lévy, F. Optical Properties of ZrS_3 and $ZrSe_3$. *Phys. B* **1981**, *105*, 169−173.
(59) Perluzzo, G.; Jandl, S.; Girard, P. E. Optical Spectra of ZrS_3. *Can. J. Phys.* **1980**, *58*, 143−145.
(60) Flores, E.; Ares, J. R.; Ferrer, I. J.; Sánchez, C. Synthesis and Characterization of a Family of Layered Trichalcogenides for Assisted Hydrogen Photogeneration. *Phys. Status Solidi RRL* **2016**, *10*, 802−806.
(61) Gorochov, O.; Katty, A.; Le Nagard, N.; Levy-Clement, C.; Redon, A.; Tributsch, H. Photoelectrochemical Behavior and Light-Induced Anodic Transformation of Zirconium Trisulfide. *J. Electrochem. Soc.* **1983**, *130*, 1301−1304.
(62) Torun, E.; Sahin, H.; Chaves, A.; Wirtz, L.; Peeters, F. M. Ab Initio and Semiempirical Modeling of Excitons and Trions in Monolayer TiS_3. *Phys. Rev. B* **2018**, *98*, 075419.

https://dx.doi.org/10.1021/acsami.0c11892
ACS Appl. Mater. Interfaces 2020, 12, 40525−40531